Chemistry and Physics of Lipids 231 (2020) 104945

Contents lists available at ScienceDirect

Chemistry and Physics of Lipids

journal homepage: www.elsevier.com/locate/chemphyslip

Refining internal bilayer structure of bicelles resolved by extended-*q* small angle X-ray scattering

Catherine Cheu[a], Lin Yang[b], Mu-Ping Nieh[a,c,d,*]

[a] Polymer Program, Institute of Materials Science, University of Connecticut, Storrs, CT 06269, USA
[b] Brookhaven National Laboratory, PO Box 5000, Upton, NY 11973-5000, USA
[c] Department of Chemical and Biomolecular Engineering, University of Connecticut, Storrs, CT 06269, USA
[d] Department of Biomedical Engineering, University of Connecticut, Storrs, CT 06269, USA

ARTICLE INFO

Keywords:
Nanodisc
Small-angle x-ray scattering
Bilayer interdigitation

ABSTRACT

The internal profile across the bilayer reveals important structural information regarding the crystallinity of acyl chains or the positions of encapsulated species. Here, we demonstrate that a simple five-layer-core-shell discoidal model can be employed to best fit the extended-*q* small angle X-ray scattering (SAXS) data and resolve the bilayer internal structure (with sub-nanometer resolution) of a nanoscale discoidal system comprised of a mixture of long- and short- chain lipids (known as "bicelles"). In contrast to the traditional core-shell discoidal model, the detailed structure in the hydrophobic core such as the methylene and methyl groups can be distinguished via this model. The refined model is validated by the SAXS data of bicelles whose electron scattering length density of the hydrophobic core is adjusted by the addition of a long-chain lipid with a fluorine-end group. The higher resolution of the bilayer internal structure can be employed to advance our understanding of the interaction and conformation of the membrane and associated molecules, such as membrane-associated proteins and locations of entrapped species in the lipid nanoparticles.

1. Introduction

Small-angle scattering (SAS) and diffraction have been applied for structural characterization of lipid bilayers, membrane-associated proteins and lipid nanoparticles for decades (Herberle et al., 2012; Angelova et al., 2017; Chaudhuri, 2015; Pan et al., 2013; Fragneto, 2012; Yaghmur and Rappolt, 2012; Kiselev, 2011; Bunjes and Unruh, 2007; Ewert et al., 2004; Winter, 2002). The former is commonly used for resolving the randomly oriented or dispersed aggregates (e.g., micelles and vesicles) with a dimension larger than 2 nm, while the latter provides the high-resolution (a few Å) structural information via reconstructing the electron (or neutron) density profile along the bilayer normal utilizing inverse Fourier Transform based on the intensities of the many-order Bragg reflections obtained from highly aligned bilayer systems (Blaurock, 1971; Engelman, 1971; Worcester and Franks, 1976; Corless, 1972; Franks, 1976; Torbet and Wilkins, 1976). It has been reported that the morphology of lipid or surfactant aggregates transforms upon environmental stimuli, e.g., variations of temperature, pH, ionic strength *etc*. (Hu et al., 2014; Bolze et al., 2000; Liu et al., 2014; Nieh et al., 2003; Mahabir et al., 2010; Nieh et al., 2011a; Li et al., 2013) and the structure can be resolved via best fitting the SAS data, where the scattering intensity is presented as a function of scattering vector, $q \equiv \frac{4\pi}{\lambda}\sin\left(\frac{\theta}{2}\right)$, where θ and λ are the scattering angle and wavelength of the probe, respectively. Kučerka et al., 2005 were able to obtain use two individual ranges of q (0.1 – 0.3 $Å^{-1}$ from diffuse scattering and 0.2 – 0.8 $Å^{-1}$ from diffraction) to obtain the structural information of unilamellar vesicle and lipid bilayers. However, the minimal q of 0.1 $Å^{-1}$ remains relatively high in comparison to the normal small angle X-ray scattering (SAXS) configuration. Simultaneous acquisition of scattering data over a wide q range allows us to use a single model (instead of combined randomly-oriented and aligned models) to yield both global and local structural information. Hence, extended-*q* small angle X-ray or neutron scattering (SAXS or SANS) data is desirable; however, the low signal-to-noise ratio (S/N) at high-q regime and the size constraint of 2-D detectors limit most SAXS or SANS from covering both low- and high- q ranges simultaneously. The newly constructed LiX instrument located at Beamline 16-ID at the National Synchrotron Light Source – II (Brookhaven National Laboratory) (DiFabio et al., 2016) has three detectors to cover the angles from low to high, resulting in a wide q range between 0.005 and 2.5 $Å^{-1}$. As a result, the detailed internal structure of a discoidal lipid micelle, known as a bicelle, can be obtained in an aqueous solution which was not

* Corresponding author at: Polymer Program, Institute of Materials Science, University of Connecticut, Storrs, CT 06269, USA.
E-mail address: mu-ping.nieh@uconn.edu (M.-P. Nieh).

https://doi.org/10.1016/j.chemphyslip.2020.104945
Received 25 April 2020; Received in revised form 18 June 2020; Accepted 26 June 2020
Available online 01 July 2020

easily achievable in the past.

The basic components of bicelles are long- and short- chain lipids, which constitute the planar and rim of size-uniform discs, respectively. Bicelles were initially designed and widely used to host the membrane-associated proteins as a substrate (Sanders and Landis, 1995; Ottiger and Bax, 1998; Struppe et al., 1998; Ottiger and Bax, 1999; Sass et al., 1999; Fischer et al., 1998; Andersson and Maler, 2002). Their flat bilayer structure resembles the native biological local low-curvature environment, allowing the structures and activities of bicelle-associated proteins to be presumably better retained in comparison with the proteins in detergent environment with high curvatures (Beaugrand et al., 2014; Dürr et al., 2012; Lind et al., 2008). Moreover, their alignability in magnetic fields enables the structural analysis of the associated proteins with preferred orientation, although later on the magnetically alignable phase were confirmed to be either perforated lamellae (charged) or bilayered ribbons (non-charged) (Nieh et al., 2002, 2004, 2011b; van Dam et al., 2004). Recently, it has been reported that discoidal bicelles show high cellular uptake, making them suitable for efficacious delivery of theranostic molecules (Aresh et al., 2016; Rodríguez et al., 2015; Rad et al., 2019a, 2019b). The location of these payloads would allow researchers to understand the organization of such biomembranes. Therefore, it is important to resolve the internal structure of the membrane-like structure. In this report, we developed a 5-layer core-shell disc (5LCSD) scattering model which better agrees with the extended-q SAXS data resulting in higher resolution for the bilayer internal structure than the previously reported core-shell discoidal (CSD) model (Nieh et al., 2002; Yang et al., 2012; Luchette et al., 2001). The 5LCSD model is further validated by bicelles which contain long-chain lipids with a fluorine atom at the end of a hydrocarbon chain to enhance the electron density of the hydrophobic region. This model can be further used to identify the location of the entrapped molecules in the well-defined lipid nanodiscs.

2. SAXS analysis

2.1. Vesicular model

A common morphology of lipid aggregates in aqueous solution is a vesicle as shown in Fig. 1 – a spherical compartment enclosed by a continuous lipid bilayer shell to separate the interior content and the exterior solution. As a bilayer is composed of amphiphilic phospholipid molecules, the hydrophilic headgroup has the highest electron density due to the heavy phosphate which normally yields a broad peak in the SAXS data at q around 0.12 $Å^{-1}$ corresponding to the bilayer thickness (i.e., phosphate-to-phosphate distance). The hydrophobic hydrocarbon tail region can be in either well-ordered gel phase or fluidic L_α phase. It is expected that these two phases should result in different scattering patterns due to the fact that the crystalline methylene region in gel phase has a higher electron density than that of the methyl end group located at the center of the bilayer as shown in Fig. 1. On the other hand, the difference in electron density between flexible methylene in L_α phase and methyl group should be reduced. Such difference is reflected in the q range larger than 0.4 $Å^{-1}$, which is difficult to resolve with accuracy in most of the general SAXS data due to low S/N ratio and limited q range. Here, the extended-q SAXS data are attainable and expected to differentiate the high- density crystalline methylene from the low-density methyl group. Our first attempt is to apply an existing 5-layer spherical shell (5LSS) model, as described below, to fit the SAXS data from bicelle solutions in order to resolve the bilayer internal structure.

The intensity profile of a sample can be simulated as a function of q as shown in Eqs. (1) and (2) (Doucet et al., 2018).

$$I(Q) = \frac{\phi}{V_t} F_{5LSS}(q)^2 + background \tag{1}$$

$$F_{5LSS}(q) = 3\left[V_c(\rho_{solv} - \rho_{s,1}) \frac{\sin(qr_c) - qr_c\cos(qr_c)}{(qr_c)^3} + \sum_{i=1}^{n-1} V_{s,i}(\rho_{s,i} - \rho_{s,i+1}) \frac{\sin(qr_{s,i}) - qr_{s,i}\cos(qr_{s,i})}{(qr_{s,i})^3} + V_t(\rho_{s,n} - \rho_{solv}) \frac{\sin(qr_{s,n}) - qr_{s,n}\cos(qr_{s,n})}{(qr_{s,n})^3} \right], \tag{2}$$

where ϕ is the volume fraction of the vesicles, ρ_{solv} and $\rho_{s,i}$ are the scattering length density of solvent and the ith shell, respectively, V_c, $V_{s,i}$ and V_t are the core and total volume, the enclosed volume by the ith shell (included), respectively, and r_c and $r_{s,i}$ are the radii of core and the ith shell, respectively.

The 5LSS model is expected to capture the features of the bilayer, i.e., capable of best fitting to the experimental SAXS data of bicelles in the high q regime when the radius of the vesicle (i.e., r_c) is set to be sufficiently large to minimize the curvature of the bilayer. However, due to the preset large r_c, this model would not be sufficient to fit the low-q regime of the SAXS data where the real size of the bicelles is revealed.

2.2. Core-Shell Discoidal (CSD) model

The CSD model has been applied for fitting to the experimental SAXS data of bicelles as previously reported by Yang et al. (2012). The mathematical expression of the form factor, $F_{CSD}(q, \alpha)$ based on the schematic shown in Fig. 2 is described in Eq. 4 (Singh, 2009).

$$I(Q) = \frac{\phi}{V_t} \int F_{CSD}(q, \alpha)^2 \sin(\alpha) d\alpha + background, \tag{3}$$

where α is the angle between the scattering vector q and the discoidal normal.

$$F_{CSD}(q, \alpha) = \left[(\rho_{core} - \rho_{shell}) V_c \frac{2J_1(qRsin\alpha)}{qRsin\alpha} \frac{\sin\left\{q\left(\frac{L}{2}\right)cos\alpha\right\}}{q\left(\frac{L}{2}\right)cos\alpha} + (\rho_{shell} - \rho_{rim}) V_{c+s} \frac{2J_1(qRsin\alpha)}{qRsin\alpha} \frac{\sin\left\{q\left[\left(\frac{L}{2}\right) + t_s\right]cos\alpha\right\}}{q\left[\left(\frac{L}{2}\right) + t_s\right]cos\alpha} + (\rho_{rim} - \rho_{solv}) V_t \frac{2J_1[q(R + t_r)sin\alpha]}{q(R + t_r)sin\alpha} \frac{\sin\left\{q\left[\left(\frac{L}{2}\right) + t_s\right]cos\alpha\right\}}{q\left[\left(\frac{L}{2}\right) + t_s\right]cos\alpha} \right], \tag{4}$$

where ρ_{core}, ρ_{shell}, ρ_{rim} and ρ_{solv} are the electron scattering length densities of the hydrophobic core, the hydrophilic shell (in the planar region), rim and solvent, respectively, R, L, t_s and t_r are the core radius and the thicknesses of the core, shell and rim, respectively, and V_c, V_{c+s} and V_t are the volume of core and (core + shell) of the disc and the whole disc, respectively. J_1 is the first-order Bessel function of the first kind.

The CSD model has demonstrated reasonable best fits to the SAXS data of bicelle solutions for the q range less than 0.2 $Å^{-1}$ (Yang et al., 2012). In this model, the hydrophobic core is considered to have a uniform electron density, ρ_{core} which is presumably valid if the lipid is in the L_α phase (i.e., melting hydrocarbon chains). It has been reported that the hydrocarbon chains of the long-chain lipid of bicelles are mostly in gel phase (Liu et al., 2014, 2017; Li et al., 2013; Nieh et al., 2011a, 2011b), where the methylene group is mostly crystalline with higher density but the methyl end group near the center of the bilayer is mobile and occupies more volume, hence having lower density. Whether the core can be treated as one uniform region would mostly affect the SAXS pattern at a higher q range. Therefore, we will use SAXS data

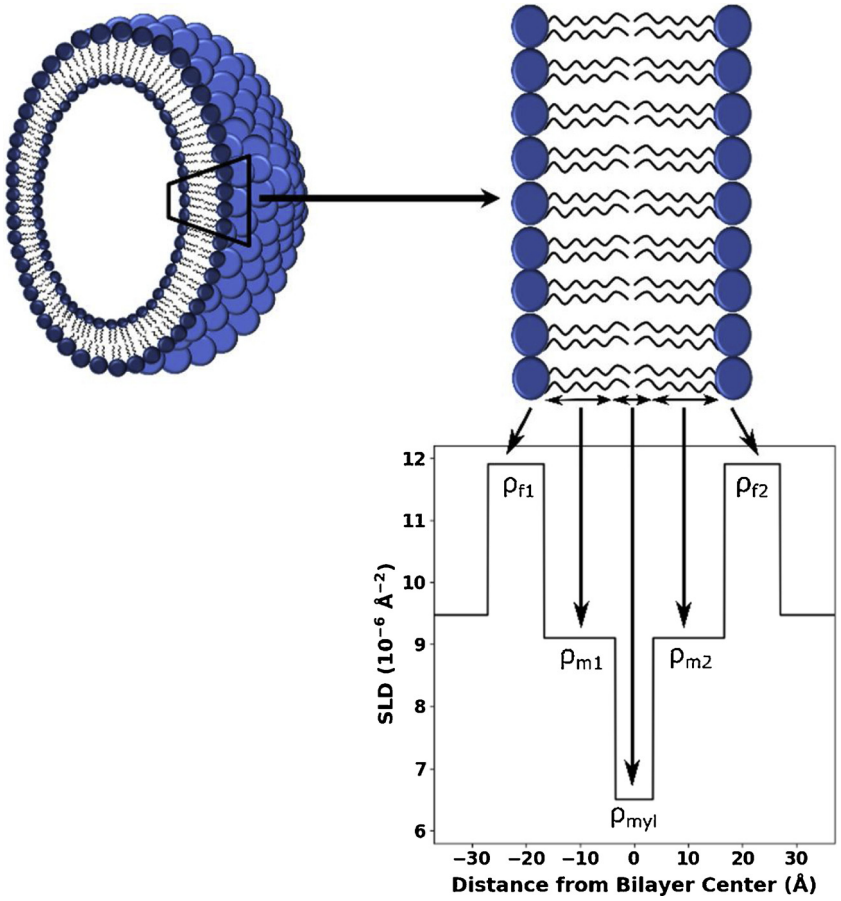

Fig. 1. The schematic of the cross-section of a vesicle (top left) and the electron density profile across the bilayer (bottom). A 5-layer spherical shell (5LSS) model can therefore be used to describe the SAXS data.

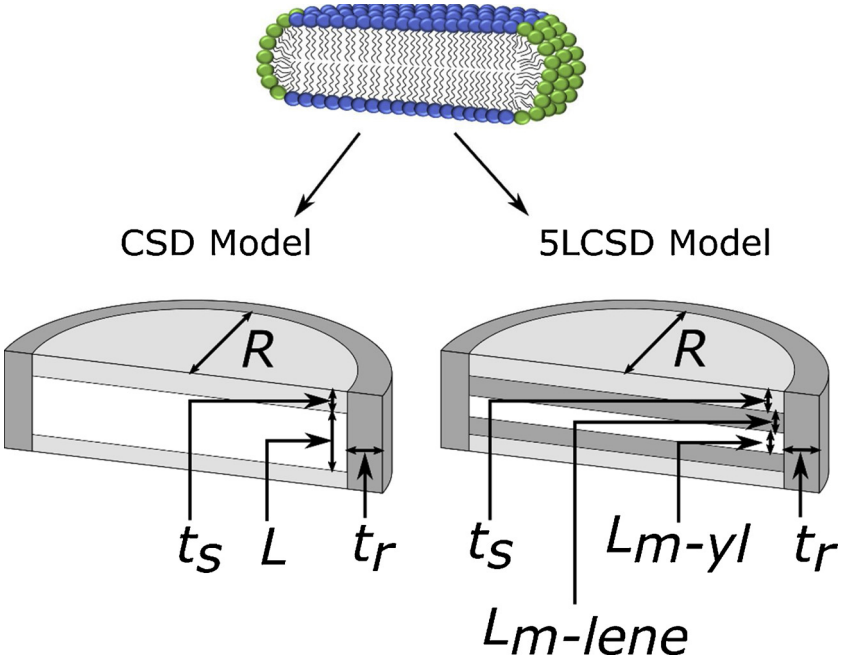

Fig. 2. The schematic of bicelle (top) where the long-chain lipid (with blue heads) and short-chain lipid (with green heads) make up the planar and rim regions of the nanodisc. The schematics of the two scattering models, CSD and 5LCSD (bottom) can be used to describe the SAXS data.

with an extended q range collected at LiX to examine the model.

2.3. 5-Layer-Core-Shell discoidal (5LCSD) model

The new 5LCSD model is derived based on the abovementioned CSD model with the hydrophobic core split into 3 layers: a methyl region sandwiched by two methylene regions as shown in Fig. 2. Together with the top and bottom shells, there are 5 layers in total. Eq. (3) remains valid for the scattering function, however the form factor should be replaced by $F_{5LCSD}(q, \alpha)$, which can be expressed by the following equation:

$$F_{5LCSD}(q,\alpha) = \left[(\rho_{m-yl} - \rho_{m-lene}) V_{m-yl} \frac{2J_1(qRsin\alpha)}{qRsin\alpha} \frac{\sin\left\{q\left(\frac{L_{m-yl}}{2}\right)cos\alpha\right\}}{q\left(\frac{L_{m-yl}}{2}\right)cos\alpha} + (\rho_{m-lene} - \rho_s) V_c \frac{2J_1(qRsin\alpha)}{qRsin\alpha} \frac{\sin\left\{q\left(\frac{L}{2}\right)cos\alpha\right\}}{q\left(\frac{L}{2}\right)cos\alpha} + (\rho_s - \rho_r) V_{c+s} \frac{2J_1(qRsin\alpha)}{qRsin\alpha} \frac{\sin\left\{q\left[\left(\frac{L}{2}\right) + t_s\right]cos\alpha\right\}}{q\left[\left(\frac{L}{2}\right) + t_s\right]cos\alpha} + (\rho_r - \rho_{solv}) V_t \frac{2J_1[q(R + t_r)sin\alpha]}{q(R + t_r)sin\alpha} \frac{\sin\left\{q\left[\left(\frac{L}{2}\right) + t_s\right]cos\alpha\right\}}{q\left[\left(\frac{L}{2}\right) + t_s\right]cos\alpha} \right], \quad (5)$$

where $\rho_{m\text{-}lene}$, $\rho_{m\text{-}yl}$, ρ_s, ρ_r are the electron density of methylene, methyl group, shell, and rim, respectively, $L_{m\text{-}yl}$ is the thickness of the methyl groups, and $V_{m\text{-}yl}$ is the volume of the methyl groups, respectively. The rest of the parameters have the same definition as those in Eq. (4). Here, $L = 2L_{m\text{-}lene} + L_{m\text{-}yl}$, where $L_{m\text{-}lene}$ is the thickness of methylene group. J_1 is the first-order Bessel function.

In this report, we will evaluate the necessity of implementing the three-layer core and its effect on the high-q regime of the SAXS data. Moreover, this model will be validated by the best fits to the extended-q SAXS data of bicelles where the electron density can be adjusted in the hydrophobic core of the bilayer. This report will demonstrate how the 5LCSD model can be used to resolve the bilayer structure as new species are introduced into the structure.

3. Experiment

3.1. Sample preparation

All lipids including long-chain 1,2-dipalmitoyl-*sn*-glycero-3-phosphocholine (DPPC), long-chain fluorine-labeled 1-palmitoyl-2-(16-fluoropalmitoyl)-*sn*-glycero-3-phosphocholine (F-DPPC), short-chain dihexanoyl phosphatidylcholine (DHPC), and charged long-chain 1,2-dipalmitoyl-sn-glycero-3-phosphoglycerol (DPPG) were purchased from Avanti Polar Lipids (Alabaster, AL) and were used without further purification. The structures of these lipids are shown in Fig. 3. DPPC, DPPG and F-DPPC are considered as the long-chain lipids and DHPC is considered as the short-chain lipid. Stock solutions of individual lipids were each first prepared by dissolving a specific amount of lipid into chloroform, while the DPPG stock solution was prepared in a chloroform/methanol mixture with a volume ratio of 65/35. Bicelles were then made by mixing the stock solutions of individual lipids at appropriate molar ratios based on Table 1, where the molar ratio of long- to short- chain lipid remained constant at 3.2 and the molar ratio of negatively charged DPPG to total long-chain lipid was also fixed at 0.01 for all samples to stabilize the nanodiscs as reported previously (Losonczi and Prestegard, 1998; Nieh et al., 2011a, 2011b; Liu et al., 2014). After the appropriate amounts of the lipid stock solutions were mixed, they were dried overnight in a vacuum oven. The dried lipid mixtures were then hydrated with deionized water to form 10 wt. % solutions, followed by a temperature cycling process to form homogeneous bicelle solutions. The standard procedure can be found elsewhere (Aresh et al., 2016; Liu et al., 2014, 2017). All the samples were further diluted into 1 wt. % for SAXS measurements.

Table 1
Molar Ratios of Bicelles.

System	DPPC mol. %	DHPC mol. %	DPPG mol. %	F-DPPC mol. %
DPPC/DHPC/DPPG	0.754	0.238	0.00762	0.000
20:80 F-DPPC:DPPC	0.603	0.238	0.00762	0.151
30:70 F-DPPC:DPPC	0.528	0.238	0.00762	0.226
40:60 F-DPPC:DPPC	0.453	0.238	0.00762	0.302

Table 2
SLD Parameters Obtained from CSD, 5LSS, and 5LCSD Models.

Parameter	CSD	5LSS	5LCSD
ρ_s (10^{-6} Å^{-2})	11.40 ± 0.05	N/A	11.9 ± 0.1
ρ_r (10^{-6} Å^{-2})	9.60 ± 0.01	N/A	9.7 ± 0.0
ρ_{core} (10^{-6} Å^{-2})	8.00 ± 0.04	N/A	N/A
$\rho_{m\text{-}ylene}$ (10^{-6} Å^{-2})	N/A	N/A	9.10 ± 0.01
$\rho_{m\text{-}yl}$ (10^{-6} Å^{-2})	N/A	N/A	6.50 ± 0.03
ρ_{f1}, ρ_{f2} (10^{-6} Å^{-2})	N/A	11.40 ± 0.03	N/A
ρ_{m1}, ρ_{m2} (10^{-6} Å^{-2})	N/A	9.40 ± 0.04	N/A
ρ_{myl} (10^{-6} Å^{-2})	N/A	7.5 ± 0.1	N/A

3.2. SAXS instrument and analysis

The SAXS experiment was performed at LiX at Beamline 16 of the National Synchrotron Light Sources –II (NSLS-II) located at Brookhaven National Laboratory (BNL). The samples were in a 15-position sample stage where the samples were sandwiched by a pair of mica sheets with

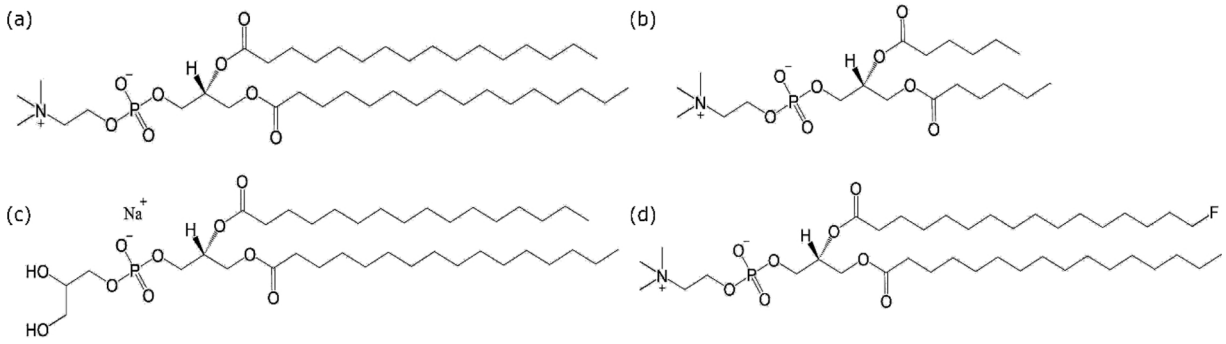

Fig. 3. Chemical Structures of Lipids: (a) DPPC, (b) DHPC, (c) DPPG, (d) F-DPPC.

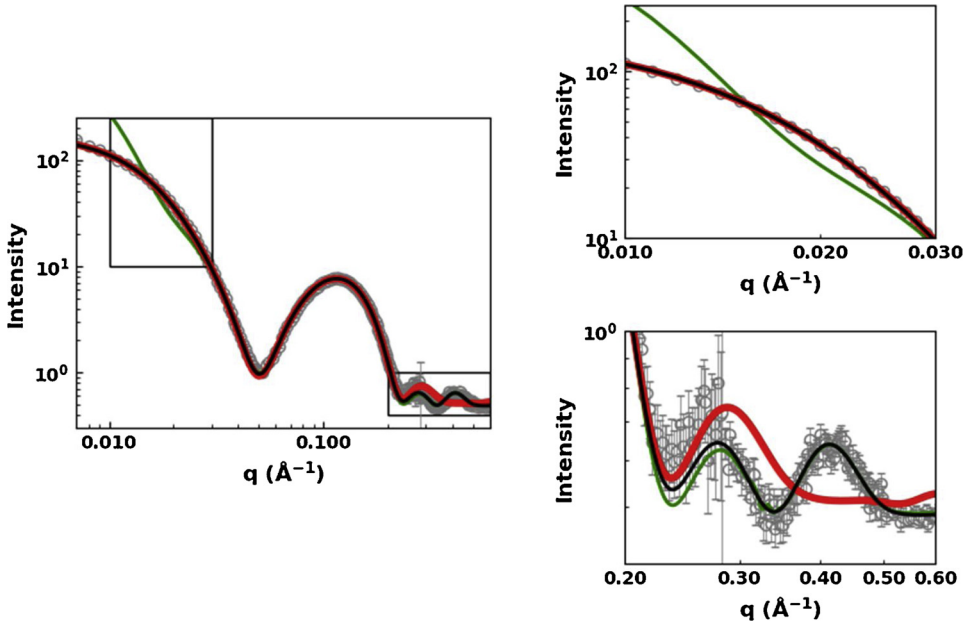

Fig. 4. The best fits to the SAXS data of DPPC/DHPC/DPPG bicelles (symbols) using three models: 5LSS (green), CSD (red) and 5LCSD (black). The insets are zoom-in plots at low q (top right) and high q (bottom right) regimes.

a well-defined gap of 2.4 mm. All samples were run at 25 °C which is below the melting transition temperature of DPPC (~ 41 °C).

The 2-D intensity data were first reduced to 1-D SAXS data as a function of q, which were then corrected by background subtraction of water scattering through matching the water peaks from the sample with that from the water. Analysis of the 5LSS and CSD scenarios were done using the core multishell model and core shell bicelle model provided from SASView 4.2.0 (Doucet et al., 2018). All three models were tested on F-DPPC-free bicelles for comparison purpose. ρ_{solv} was set as a constant of 9.47 × 10^{-6}Å^{-2}, the calculated electron scattering length density for water. Polydispersity (PDI), defined as $\frac{\sigma_x}{\langle x \rangle}$, where σ_x and $< x >$ are standard deviation and average of variable x, respectively, using a Schulz distribution (Kotlarchyk and Chen, 1983) were incorporated in the 5LCSD model to describe the radius for all samples as well as the shell thickness for the 40 mol% F-DPPC sample. All automated fitting parameters for 0–30 mol% F-DPPC samples are listed in the Supplementary Information Tables S1 – S3.

4. Fitting results

4.1. Comparison among 5LSS, CSD and 5LCSD models

Fig. 4 illustrates the general SAXS pattern from DPPC/DHPC/DPPG bicelles. A slope transition takes place around 0.02 Å^{-1}, indicating the end of the Guinier regime, where $q{\cdot}L < 1$ and L is the largest dimension, i.e., $[(R + t_r)]$ in the case of a bicelle. After the decay, three broad peaks are observed at q between 0.06 and 0.6 Å^{-1}, presumably corresponding to the internal structure of the bilayer. First, the CSD model was applied to fit the SAXS data, yielding a reasonable fit over the q range between 0.008 and 0.32 Å^{-1}. However, at $q >$ 0.35 Å^{-1}, the CSD model can no longer satisfactorily fit the data, especially the third peak at q ~ 0.4 Å^{-1} which cannot be simulated by this model (the bottom inset of Fig. 4), suggesting a model with a more detailed structure is needed. We speculated that the electron density of the core cannot be assumed uniform throughout the hydrophobic regime because of the differences in the volumetric densities between the crystalline methylene and the mobile methyl end groups. An attempt for proof-of-concept is to fit the SAXS data in the extended-q range with the aforementioned 5LSS model with an extremely large r_c (minimizing the curvature effect), whose five-layer shells are made of the phosphate headgroup (s1) – methylene (s2) – methyl (s3) – methylene (s4) – phosphate headgroup (s5) from inner to outer leaflet in sequence where the electron density and thickness of s1 and s2 are identical to those of s5 and s4, respectively. The 5LSS model can indeed successfully simulate the three peaks at the high-q regime of the SAXS data but completely mismatch with the data at the low-q regime (the top inset of Fig. 4) due to the wrong morphology. The aforementioned 5LCSD model, a modified version of CSD model with three core layers (five layers in total with two phosphate shells), is therefore required to fit the data over the extended-q range.

The best fit using the 5LCSD model as shown in Fig. 4 shows good agreement with the SAXS data throughout the whole q range (from 0.007 to 0.6 Å^{-1}), validating the model. In Table 4, the best fitting $\rho_{m\text{-}lene}$ and $\rho_{m\text{-}yl}$ are 9.1 × 10^{-6} and 6.5 × 10^{-6} Å^{-2}, respectively, lower than ρ_{solv} (9.47 × 10^{-6} Å^{-2}) and consistent with the expected density variation in the core. Moreover, the best fitting value of ρ_{core} from CSD model falls between the best fitting $\rho_{m\text{-}lene}$ and $\rho_{m\text{-}yl}$, showing excellent consistency of the two models (5LCSD and CSD). The total bilayer thickness from the best fitting result of (54 ± 2.2) Å (Table 3) falls in the range between the reported steric bilayer thickness of gel-phase DPPC of 52.4 Å (Nagle and Tristram-Nagle, 2000) obtained through diffraction at 20 °C and the reported bicellar bilayer thickness of 55.3 Å fitted using the CSD model (Yang et al., 2012), and very close to the best fitting bilayer thickness from the 5LSS model, 53.5 ± 1.4 Å in Table 3. It is noteworthy that the best fitting $t_{m\text{-}yl}$ appears to be larger than the expected methyl group, implying that the low-density mobile region extends to a few CH_2- units toward the center of the bilayer core.

In Section 4.2, we will further verify the 5LCSD model using bicelles containing F-DPPC which presumably changes the electron density profile of the hydrophobic core in the bilayer.

4.2. Validation of 5LCSD model via SAXS of F-DPPC/DPPC bicelles

Fig. 5 shows the SAXS data of the bicelles containing F-DPPC with different compositions. For samples containing up to 30 mol% of F-DPPC (30:70 F-DPPC:DPPC), the scattering patterns inherit the features of the 0:100 F-DPPC:DPPC bicelle scattering pattern with all three peaks present but less pronounced. The best fits using 5LCSD model are in good agreement with the SAXS data and all values for the fitting parameters of all samples are listed in Table 4. The most obvious effect of F-DPPC on the morphology of bicelles is that the core radius

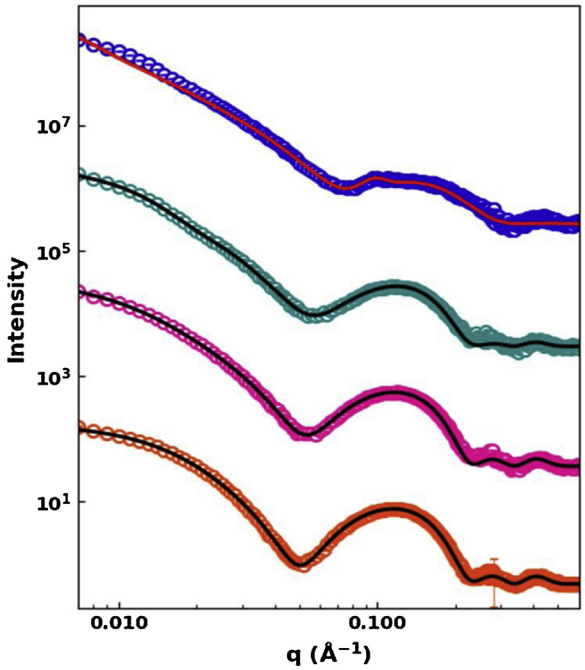

Fig. 5. The SAXS data of F-DPPC/DPPC bicelles with F-DPPC:DPPC = 0:100 (orange), 20:80 (pink), 30:70 (dark cyan) and 40:60 (blue). The black solid curves are best fits of F-DPPC:DPPC = 0:100, 20:80 and 30:70 using 5LCSD model and the red solid curve is the manual fits of F-DPPC:DPPC = 40:60 using the 5LCSD model plus a Gaussian peak that simulates the multilayered vesicle structure with the parameters listed in Table 4. SAXS data containing F-DPPC were rescaled for clarity.

increased as the F-DPPC content in the bicelle increased. This is presumably attributed to the variation of the packing parameter of DPPC upon mixing with F-DPPC. The reduction of the best fitting ρ_s as shown in Table 4, is likely caused by two possible contributing factors: (1) more water associates with the phosphate headgroup caused by more space between adjacent lipids due to the insertion of fluorine atoms in the bilayer, (2) the F-DPPC containing bilayer may perturb the headgroup alignment vertical to the bilayer, making the headgroup shell taking into account of some water and a portion of methylene groups.

The methyl fluorine located at the end of the lipid acyl chain has a higher electron density than hydrogen. The contrast in electron density, $(\rho_{m\text{-}lene} - \rho_{m\text{-}yl})$, should decrease under the condition that the headgroup of F-DPPC aligns with that of DPPC, i.e., no disturbance for the DPPC bilayer. This can be confirmed by the following two observations: (1) the similarity of scattering patterns from the samples with F-DPPC:DPPC ≤ 30:70 and (2) the total bilayer thickness from the best fits, i.e., $[2(t_s + L_{m\text{-}lene}) + L_{m\text{-}yl}]$ are practically invariant with the composition of F-DPPC within the statistic errors. From the best fits, $(\rho_{m\text{-}lene} - \rho_{m\text{-}yl})$ has reduced from 2.6×10^{-6} to 1.6×10^{-6} Å^{-2} as the molar ratio of F-DPPC:DPPC increased from 0:100 to 30:70 (Table 4). Further increase of the F-DPPC composition caused the deviation of the typical three-peak SAXS pattern to the smeared two-peak feature, indicating that the bilayer structure might be disturbed. It is noteworthy that the SAXS data of bicelles containing a F-DPPC:DPPC molar ratio of 40:60 also shows a hidden sharp peak at ~ 0.1 Å^{-1} (Fig. 5) – a scattering feature characteristic of multilamellar vesicles (MLVs), implying that over-doped F-DPPC in the bicelles may yield MLVs.

In addition, it was found that the best fit to the 40:60 data did not agree with the data as well as the best fits in for other samples. This is likely attributed to the bilayer interdigitation induced by F-DPPC as Smith et al. has suggested (2010). Finally, the increased value of the best fitting t_r with increasing F-DPPC molar ratio (for F-DDPC:DPPC ≤ 30:70) seemingly suggests that some of long-chain F-DPPC molecules may participate in the short-chain DHPC-rich rim, resulting in an increase of the rim thickness. However, further experiments are needed to verify this statement.

Table 3
Best Fitting Dimensions Obtained from CSD, 5LSS, and 5LCSD Models of bicelles.

Parameter	CSD	5LSS	5LCSD
***R*(Å)**	79.3 ± 2.1	102.8 ± 1.4	81.0 ± 1.9
t_s (Å)	15.0 ± 0.1	N/A	10.3 ± 0.2
t_r (Å)	54.7 ± 2.4	N/A	53.1 ± 2.3
t_{core} (Å)	26.0 ± 0.1	N/A	33.4 ± 1.8 (calc.)
$L_{m\text{-}ylene}$ (Å)	N/A	N/A	13.2 ± 0.4
$L_{m\text{-}yl}$ (Å)	N/A	N/A	7.0 ± 1.0
r_{f1} (Å)	N/A	10.1	N/A
r_{m1} (Å)	N/A	12.6	N/A
r_{myl} (Å)	N/A	8.1 ± 0.9	N/A
r_{m2} (Å)	N/A	12.6 ± 0.3	N/A
r_{f2} (Å)	N/A	10.1 ± 0.2	N/A
***PDI* (*R*)**	0.42 ± 0.02	0.45 ± 0.02	0.40 ± 0.02

Table 4
Parameter estimates of F-DPPC/DPPC bicelles using the 5LCSD model; (ρ_{solv} = 9.47 × 10^{-6}Å^{-2}).

	F-DPPC:DPPC Molar Ratio			
Fitting Parameter	0:100	20:80	30:70	40:60*
***R* (Å)**	81.0 ± 1.9	95.7 ± 2.7	131.2 ± 2.2	260.0
$\rho_{m\text{-}lene}$ (10^{-6} Å^{-2})	9.1 ± 0.0	9.3 ± 0.0	9.5 ± 0.1	8.8
$\rho_{m\text{-}yl}$ (10^{-6} Å^{-2})	6.5 ± 0.3	7.1 ± 0.3	7.9 ± 0.3	8.8
ρ_s (10^{-6} Å^{-2})	11.9 ± 0.1	11.4 ± 0.0	10.8 ± 0.1	10.3
ρ_r (10^{-6} Å^{-2})	9.7 ± 0.0	9.7 ± 0.0	9.7 ± 0.0	9.8
t_s (Å)	10.3 ± 0.2	10.4 ± 0.3	10.3 ± 0.8	11.6
t_r (Å)	53.1 ± 2.3	60.1 ± 2.1	71.6 ± 2.7	90.0
$L_{m\text{-}lene}$ (Å)	13.2 ± 0.4	13.1 ± 0.5	12.2 ± 0.6	8.0
$L_{m\text{-}yl}$ (Å)	7.0 ± 1.0	6.8 ± 1.4	8.7 ± 2.3	2.0
***PDI* (*R*)**	0.40 ± 0.02	0.56 ± 0.02	0.22 ± 0.02	0.3
***PDI* (t_s)**				0.42
***Gaussian Peak Position* (Å^{-1})**				0.097
***σ* (standard deviation)**				0.01

* SAXS data of sample 40:60 were fitted by manually adjusting the parameters.

5. Discussions

Over decades, SAXS and SANS have been powerful techniques to resolve nanostructures with a length scale larger than 2 nm. The constraint on insufficient resolution at the smaller length scale (< 2 nm) is mainly attributed to the low S/N ratio for the data in the high *q* regime. It has been an emergent need to combine SAXS and WAXS outcomes to provide a comprehensive understanding of the system over a wider range of length scale. The current SAXS data with the extended *q* range enables more refined models to provide higher resolution of structures. In comparing the three SAXS models (5LSS, CSD and 5LCSD) in this report, the use of the 5LCSD model demonstrates the importance of using an extended *q* range for higher resolution of sub-nanometer structures. The main purpose of using the 5LCSD model to describe the SAXS data using a single model is to render relatively accurate dimensions and electron densities of the bicellar internal structure through the best fitting over a wide range. Although both 5LSS and CSD models fit the SAXS data reasonably well over a specific *q* range yielding similar best fitting parameters, it is required to have sufficient separation between the dimensions of the two structures with no evident cross-contamination of scattering intensity from each other, which is not needed for the use of 5LCSD model.

It is noteworthy that the refined 5LCSD model has two additional

fitting parameters – $t_{m\text{-}yl}$ and $\rho_{m\text{-}yl}$ – in comparison with the CSD model. To ensure that the obtained best fitting parameters correspond to the real structures while having physical meaning, the initial guesses for the parameters describing the bilayer internal structure and contrasts were adopted from the 5LSS model, while the CSD model provided the initial guesses for the core radius and other parameters related to the rim section. During the fitting procedure, a few parameters that would not be expected to have significant changes in comparison with the DPPC bicelles, such as t_s and ρ_s were highly constrained within a narrow range of variation. Eventually, the final best fits can be obtained by slowly relaxing the constraints of all parameters. For the bicelle sample containing 40 mol% of F-DPPC, the task of performing an automated fit was found to be not feasible for using a larger number of parameters than that used for the other samples. As such, the sample data was fitted manually while maintaining reasonable values for all parameters except for ρ_{solv}.

The comparison between the electron profile across the bilayer in 5LCSD model and the electron density profile obtained from the diffraction analysis of F-DPPC bilayers provides some insight into the effect of F-DPPC in the bilayer section of the bicelle. Hirsh et al. had discovered that F-DPPC bilayers are thinner than the DPPC bilayers, and that the headgroups of oppositely oriented F-DPPC molecules were slightly closer together than their DPPC counterparts (Hirsh et al., 1998). In F-DPPC interdigitated domains, the fluorine atoms would be situated near the headgroups resulting in domains with shorter thicknesses than that of the non-interdigitated domains. As shown in Fig. 6, when F-DPPC was mixed with DPPC, a lipid which does not naturally interdigitate in the presence of water, mixed domains of both interdigitated and non-interdigitated bilayers could form as shown through DSC experiments of F-DPPC/DPPC bilayers by Smith et al. (2010). Such mixing behavior could explain the decrease in ρ_s with increasing F-DPPC content as shown in Table 4 since the slightly bulky fluorine (than hydrogen) may create more space between the lipids for water (of lower scattering length density) to participate in the headgroup region, consequently reducing ρ_s. No statistically observable changes in the t_s upon the addition of F-DPPC (up to 30 mol%) also suggest undisturbed bilayer thickness. From the fitting parameters, it appears that addition of F-DPPC up to 30 mol% results in a bilayer which appears as the middle case in Fig. 6, while the use of 40 mol% F-DPPC likely leads to a bilayer structure shown in the right case where segregated interdigitated domains could take place.

It has been reported that the increasing rates of T_M for DPPC/F-DPPC vesicles were 0.03 °C and 0.11 °C per 1 mol% increment of F-DPPC below and above 40 mol% F-DPPC, respectively (Smith et al., 2010), suggesting a morphological change of the bilayer at around 40 mol% of F-DPPC that changes the increasing rate of T_M. This is consistent with the fact that the SAXS pattern starts to change when the F-DPPC:DPPC molar ratio is 40:60, agreeing with the aforementioned thinner bilayer thickness and reduced $L_{m\text{-}yl}$ obtained from the best fitting result in Table 4. We speculate that interdigitation of the F-DPPC may occur at this composition, making the best fitting methyl layer almost disappear and the first peak almost merge with the second peak to a higher q range.

Skar-Gislinge and Arleth (2011) have applied the same strategy to differentiate the methyl and methylene regions to construct a scattering model to describe SAXS and small angle neutron scattering data of dilauroyl-phosphatidylcholine (DLPC) nanodiscs, whose rim consists of a membrane scaffold protein (MSP) belt and histine tags. They have successfully obtained the dimension of each region of the nanodiscs. The model is more complicated than ours since it also includes a polymer scattering model to account for the MSP. The SAXS data of bicellar nanodiscs yield a cleaner pattern without the contaminating signal from the MSP. Likewise, Midtgaard et al. (2014) have modelled 18A:DMPC nanodiscs using a similar model containing headgroup, methylene and methyl regions for the bilayer and a protein belt (2014). It is also reported that continuous electron density profiles across the bilayer can be applied to describe the SAXS patterns of nanodiscoidal systems, e.g., DPPC/MSP1D1, DPPC/MSP1E3D1, DMPC/MSP1D1 and DMPC/MSP1E3D1 (Graziano et al., 2018). However, the best fits do not always agree with the SAXS data throughout the full q range. With fewer fitting parameters, our model is able to yield the best fits reasonably consistent with the SAXS data and to provide physically meaningful internal structure of the nanodiscs. In addition, our model is validated by the best fits for the SAXS data of bicelles containing F-DPPC.

For both CSD and 5LCSD models, the best fit rim thickness was found to be significantly larger than the lengths of DHPC and DPPC molecules. This implies that the "rim" of discoidal bicelle may not have ideal, clear boundary as depicted in the schematic of Fig. 2. A more realistic portrayal of the rim should contain a less-dense mixture of DPPC and DHPC (in contrast to gel-phase planar DPPC), both of which are presumably in the L_α phase and/or loosely associated with water, resulting in the distinct contrast between rim and other regions of bicelles. This explanation agrees with a recent report indicating that the lipid transfer rate of DPPC between bicelles is two orders of magnitude higher than that between liposomes (Xia et al., 2015, 2016). The enhanced lipid transfer rate was presumably attributed to the DPPC at the vicinity of the rim, consistent with the large loosely-packed "rim" region obtained from this study.

The fact that increased F-DPPC content leads to further increase of the rim thickness (from 53 to 72 Å) suggests that the perturbations of the bilayer would drive more non-gel phase DPPC to the loosely packed "rim". Moreover, the fluorine atom at the end of the lipid tail is presumably more hydrophilic, and consequently F-DPPC molecules may also participate in the rim region. Both may contribute to the broadening of the rim thickness.

6. Summary

The combination of extended-q SAXS data and application of the 5LCSD model has successfully refined the internal bilayer structure of the bicelles and has been validated by the F-DPPC/DPPC bicellar system. This approach does not require the analysis of inverse Fourier transform to reconstruct the electron density profile using the diffraction peak intensity from stacked aligned lipid membranes. The higher-resolution structural information obtained from SAXS can be generally applied to the analysis of completely isotropic discoidal nanoparticles, revealing their internal structures. As a result, complete *in-situ* measurements are achievable, enabling the structural study of membrane-associated proteins or entrapped species in their native state and presenting an opportunity for obtaining fundamental understanding of biomolecule-lipid interactions.

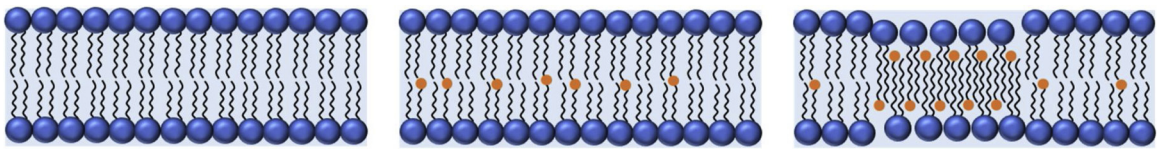

Fig. 6. Non-interdigitated DPPC bilayer (Left), non-interdigitated F-DPPC/DPPC bilayer (Middle), and segregated interdigitated and non-interdigitated bilayer (Right).

Acknowledgements

C.C. would like to thank the funding support from the Graduate Assistantship in Areas of National Needs (P200A180065), U.S. Department of Education. The project was also partially supported by NSF-CBET (1605971). The authors also would like to acknowledge the beamtime of 16ID-LiX at the NSLS-II (Brookhaven National Lab) through a beamtime proposal (BAG-302208). The LiX beamline is part of the Life Science Biomedical Technology Research resource, jointly supported by the National Institute of Health, National Institute of General Medical Sciences under Grant P41 GM111244, and by the Department of Energy Office of Biological and Environmental Research under Grant KP1605010, with additional support from NIH Grant S10 OD012331. NSLS-II is a U.S. Department of Energy (DOE) Office of Science User Facility operated for the DOE Office of Science by Brookhaven National Laboratory under Contract No. DE-SC0012704. This work benefited from the use of the SasView application, originally developed under NSF award DMR-0520547. SasView contains code developed with funding from the European Union's Horizon 2020 research and innovation programme under the SINE2020 project, grant agreement No 654000.

Appendix A. Supplementary data

Supplementary material related to this article can be found, in the online version, at doi:https://doi.org/10.1016/j.chemphyslip.2020.104945.

References

Andersson, A., Maler, L., 2002. NMR solution structure and dynamics of motilin in isotropic phospholipid bicellar solution. J. Biomol. NMR 24 (2), 103–112.
Angelova, A., Garamus, V.M., Angelov, B., Tian, Z., Li, Y., Zou, A., 2017. Advances in structural design of lipid-based nanoparticle carriers for delivery of macromolecular drugs, phytochemicals and anti-tumor agents. Adv. Colloid Interface Sci. 249, 331–345.
Aresh, W., Liu, Y., Sine, J., Thayer, D., Puri, A., Huang, Y., Wang, Y., Nieh, M.-P., 2016. The morphology of self-assembled lipid-based nanoparticles affects their uptake by Cancer cells. J. Biomed. Nanotechnol. 12 (10), 1852–1863.
Beaugrand, M., Arnold, A.A., Henin, J., Warschawski, D.E., Williamson, P.T., Marcotte, I., 2014. Lipid concentration and molar ratio boundaries for the use of isotropic bicelles. Langmuir 30 (21), 6162–6170.
Blaurock, A.E., 1971. Structure of the nerve myelin membrane: proof of the low-resolution profile. J. Mol. Biol. 56 (1), 35–52.
Bolze, J., Fujisawa, T., Nagao, T., Norisada, K., Saito, H., Naito, A., 2000. Small angle X-ray scattering and 31P NMR studies on the phase behavior of phospholipid bilayered mixed micelles. Chem. Phys. Lett. 329, 215–220.
Bunjes, H., Unruh, T., 2007. Characterization of lipid nanoparticles by differential scanning calorimetry, X-ray and neutron scattering. Adv. Drug Deliv. Rev. 59 (6), 379–402.
Chaudhuri, B.N., 2015. Emerging applications of small angle solution scattering in structural biology. Protein Sci. 24 (3), 267–276.
Corless, J.M., 1972. Biological sciences: lamellar structure of bleached and unbleached rod photoreceptor membranes. Nature 237, 229–231.
DiFabio, J., Chodankar, S., Pjerov, S., Jakoncic, J., Lucas, M., Krywka, C., Graziano, V., Yang, L., 2016. The life science x-ray scattering beamline at NSLS-II. AIP Conference Proceedings 1741, 030049.
Doucet, M., Cho, J.H., Alina, G., Bakker, J., Bouwman, W., Butler, P., Campbell, K., Gonzales, M., Heenan, R., Jackson, A., Juhas, P., King, S., Kienzle, P., Krzywon, J., Markvardsen, A., Nielsen, T., O'Driscoll, L., Potrzebowski, W., Ferraz Leal, R., Richter, T., Rozycko, P., Snow, T., Washington, A., 2018. SasView Version 4.2. https://doi.org/10.5281/zenodo.1412041.
Dürr, U.H., Gildenberg, M., Ramamoorthy, A., 2012. The magic of bicelles lights up membrane protein structure. Chem. Rev. 112, 6054–6074.
Engelman, D.M., 1971. Lipid bilayer structure in the membrane of Mycoplasma laidlawii. J. Mol. Biol. 58 (1), 153–165.
Ewert, K., Slack, N.L., Ahmad, A., Evans, H.M., Lin, A.J., Samuel, C.E., Safinya, C.R., 2004. Cationic lipid-DNA complexes for gene therapy: understanding the relationship between complex structure and gene delivery pathways at the molecular level. Curr. Med. Chem. 11 (2), 133–149.
Fischer, M.W., Losonczi, J.A., Weaver, J.L., Prestegard, J.H., 1998. Domain orientation and dynamics in multidomain proteins from residual dipolar couplings. Biochemistry 38 (28), 9013–9022.
Fragneto, G., 2012. Neutrons and model membranes. Eur. Phys. J. Special Topics 213, 327–342.
Franks, N.P., 1976. Structural analysis of hydrated egg lecithin and cholesterol bilayers I. X-ray diffraction. J. Mol. Biol. 100 (3), 345–358.
Graziano, V., Miller, L., Yang, L., 2018. Interpretation of solution scattering data from lipid nanodiscs. J. Appl. Cryst. 51, 157–166.
Herberle, F.A., Pan, J., Standaert, R.F., Drazba, P., Kucerka, N., Katsaras, J., 2012. Model-based approaches for the determination of lipid bilayer structure from small-angle neutron and X-ray scattering data. Eur. Biophys. J. 41, 875–890.
Hirsh, D.J., Lazaro, N., Wright, L.R., Boggs, J.M., McIntosh, T.J., Schaefer, J., Blazyk, J., 1998. A new monofluorinated phosphatidylcholine forms interdigitated bilayers. Biophys. J. 75, 1858–1868.
Hu, A., Fan, T.-H., Katsaras, J., Xia, Y., Li, M., Nieh, M.-p., 2014. Lipid-based nanodiscs as models for studying mesoscale coalescence – a transport limited case. Soft Matter 10, 5055–5060.
Kiselev, M.A., 2011. Methods for lipid nanostructure investigation at neutron and synchrotron sources. Phys. Part. Nucl. Lett. 42 (2), 302–331.
Kotlarchyk, M., Chen, S.-H., 1983. Analysis of small angle neutron scattering spectra from polydisperse interacting colloids. J. Chem. Phys. 79 (5), 2461–2469.
Kučerka, N., Liu, Y., Chu, N., Petrache, H.I., Tristram-Nagle, S., Nagle, J.F., 2005. Structure of fully hydrated fluid phase DMPC and DLPC lipid bilayers using X-Ray scattering from oriented multilamellar arrays and from Unilamellar Vesicles. Biophys. J. 88, 2626–2637.
Li, M., Morales, H.H., Katsaras, J., Kucerka, N., Yang, Y., Macdonald, P.M., Nieh, M.-P., 2013. Morphological characterization of DMPC/CHAPSO bicellar mixtures: a combined SANS and NMR study. Langmuir 29 (51), 15943–15957.
Lind, J., Nordin, J., Mäler, L., 2008. Lipid dynamics in fast-tumbling bicelles with varying bilayer thickness: effect of model transmembrane peptides. Biochim. Biophys. Acta 1778, 2526–2534.
Liu, Y., Li, M., Yang, Y., Xia, Y., Nieh, M.-P., 2014. The effects of temperature, salinity, concentration and PEGylated lipid on the spontaneous nanostructures of bicellar mixtures. Biochim. Biophys. Acta 1838 (7), 1871–1880.
Liu, Y., Xia, Y., Rad, A.T., Aresh, W., Nieh, M.-P., 2017. Stable discoidal bicelles: a platform of lipid nanocarriers for cellular delivery. Methods Mol. Biol. 1522, 273–282.
Losonczi, J.A., Prestegard, J.H., 1998. Imporved dilute bicelle solutions for high-resolution NMR of biological macromolecules. J. Biomol. NMR 12, 447–451.
Luchette, P.A., Vetman, T.N., Prosser, R.S., Hancock, R.E., Nieh, M.-P., Glinka, C.J., et al., 2001. Morphology of fast-tumbling bicelles: a small angle neutron scattering and NMR study. Biochim. Biophys. Acta 1513, 83–894.
Mahabir, S., Wan, W., Katsaras, J., Nieh, M.-P., 2010. Effects of charge density and thermal history on the morphologies of spontaneously formed unilamellar vesicles. J. Phys. Chem. B 114 (17), 5729–5735.
Midtgaard, S.R., Pedersen, M.C., Kirkensgaard, J.J., Sorensen, K.K., Mortensen, K., Jensen, K.J., Arleth, L., 2014. Self-assembling peptides form nanodiscs that stabilize membrane proteins. Soft Matter 10, 738.
Nagle, J.F., Tristram-Nagle, S., 2000. Structure of lipid bilayers. Biochim. Biophys. Acta 1469, 159–195.
Nieh, M.-P., Glinka, C., Krueger, S., Prosser, R., Katsaras, J., 2002. SANS study on the effect of lanthanide ions and charged lipids on the morphology of phospholipid mixtures. Biophys. J. 82, 2487–2498.
Nieh, M.-P., Harroun, T.A., Raghunathan, V.A., Glinka, C.J., Katsaras, J., 2003. Concentration-independent spontaneously forming biomimetric vesicles. Phys. Rev. Lett. 91, 158105.
Nieh, M.-P., Raghunathan, V.A., Glinka, C.J., Harroun, T.A., Pabst, G., Katsaras, J., 2004. The magnetically alignable phase of phospholipid "bicelle" mixtures in a chiral nematic made up of worm-like micelles. Langmuir 20, 7893–7897.
Nieh, M.-P., Dolinar, P., Kucerka, N., Kline, S.R., Debeer-Schmitt, L.M., Littrell, K.C., Katsaras, J., 2011a. Formation of kinetically trapped nanoscopic unilamellar vesicles from metastable nanodiscs. Langmuir 27 (33), 14308–14316.
Nieh, M.-P., Raghunathan, V.A., Pabst, G., Harroun, T., Nagashima, K., Morales, H., et al., 2011b. Temperature driven annealing of perforations in bicellar model membranes. Langmuir 27 (8), 4838–4847.
Ottiger, M., Bax, A., 1998. Characterization of magnetically oriented phospholipid micelles for measurement of dipolar couplings in macromolecules. J. Biomol. NMR 12, 361–372.
Ottiger, M., Bax, A., 1999. Bicelle-based liquid crystals for NMR-measurement of dipolar couplings at acidic and basic pH values. J. Biomol. NMR 13, 187–191.
Pan, J., Heberle, F.A., Petruzielo, R.S., Katsaras, J., 2013. Using small-angle neutron scattering to detect nanoscopic lipid domains. Chem. Phys. Lipids 170-171, 19–32.
Rad, A.T., Chen, C.-W., Aresh, W., Xia, Y., Lai, P.-S., Nieh, M.-P., 2019a. Combinational effects of active targeting, shape, and enhanced permeability and retention for Cancer theranostic nanocarriers. ACS Appl. Mater. Interfaces 11, 10505–10519.
Rad, A.T., Malik, S., Yang, L., Oberoi-Khanuja, T.K., Nieh, M.-P., Bahal, R., 2019b. A universal discoidal nanoplatform for the intracellular delivery of PNAs. Nanoscale 11 (26), 12399–12726.
Rodríguez, G., Barbosa-Barros, L., Rubio, L., Cócera, M., Fernández-Campos, F., Calpena, A., et al., 2015. Bicelles: new lipid nanosystems for dermatological applications. J. Biomed. Nanotechnol. 11 (2), 282–290.
Sanders, C.R., Landis, G.C., 1995. Reconstitution of membrane proteins into lipid-rich bilayered mixed micelles for NMR studies. Biochemistry 34 (12), 4030–4040.
Sass, J., Cordier, F., Hoffmann, A., Rogowski, M., Cousin, A., Omichinski, J.G., et al., 1999. Purple membrane induced alignment of biological macromolecules in the magnetic field. J. Am. Chem. Soc. 121 (10), 2047–2055.
Singh, D., 2009. Small Angle Scatting Studies of Self Assembly in Lipid Mixtures. [Order No. 3340003]. The Johns Hopkins University.
Skar-Gislinge, N., Arleth, L., 2011. Small-angle scattering from phospholipid nanodiscs: derivation and refinement of a molecular constrained analytical model form factor. Phys. Chem. Chem. Phys. 13, 3161–3170.

Smith, E.A., van Gorkum, C.M., Dea, P.K., 2010. Properties of phosphatidylcholine in the presence of its monofluorinated analogue. Biophys. Chem. 147, 20–27.
Struppe, J., Komives, E.A., Taylor, S.S., Vold, R.R., 1998. 2H NMR studies of a myristoylated peptide in neutral and acidic phospholipid bicelles. Biochemistry 37 (44), 15523–15527.
Torbet, J., Wilkins, M.H., 1976. X-ray diffraction studies of lecithin bilayers. J. Theor. Biol. 62 (2), 447–458.
van Dam, L., Karlsson, G., Edwards, K., 2004. Direct observation and characterization of DMPC/DHPC aggregates under conditions relevant for biological solution NMR. Biochim. Biophys. Acta Biomembr. 1664 (2), 241–256.
Winter, R., 2002. Synchrotron X-ray and neutron small-angle scattering of lyotropic lipid mesophases, model biomembranes and proteins in solution at high pressure. Biochim. Biophys. Acta Protein Struct. Mol. Enzymol. 1595 (1-2), 160–184.
Worcester, D., Franks, N., 1976. Structural analysis of hydrated egg lecithin and cholesterol bilayers. J. Mol. Biol. 100, 359–378.
Xia, Y., Li, M., Charubin, K., Liu, Y., Heberle, F.A., Katsaras, J., et al., 2015. Effects of Nanoparticle Morphology and Acyl Chain Length on Spontaneous Lipid Transfer Rates. Langmuir 31, 12920–12928.
Xia, Y., Charubin, K., Marquardt, D., Heberle, F.A., Katsaras, J., Tian, J., et al., 2016. Morphology-induced defects enhance lipid transfer rates. Langmuir 32, 9757–99764.
Yaghmur, A., Rappolt, M., 2012. Structural characterization of lipidic systems under nonequilibrium conditions. Eur. Biophys. J. 41 (10), 831–840.
Yang, P.-W., Lin, T.-L., Hu, Y., Jeng, U.-S., 2012. Small-angle X-ray scattering studies on the structure of mixed DPPC/diC7PC micelles in aqueous solutions. Chin. J. Phys. 50 (2), 349–356.